Journal of Structural Geology, Vol. 14, No. 10, pp. 1111 to 1120, 1992
Printed in Great Britain

0191-8141/92 $05.00+0.00

Stress spaces and stress paths

WILLIAM R. JAMISON

Centre for Earth Resources Research, Department of Earth Sciences, Memorial University of Newfoundland, St John's, Newfoundland, Canada A1B 3X5

(*Received* 2 *August* 1991; *accepted in revised form* 31 *March* 1992)

Abstract—The stress history, or stress path, of a rock is determined by burial and lithification, regional tectonics, local structural development, pore fluid pressure variations, etc. The cumulative effect of these influences can produce stress conditions that are not readily anticipated, and which can be quite variable across a single geological structure. A complex stress history can be more clearly represented in such alternative presentations as J space, p–q space and σ space than in the familiar Mohr space format. Stress state and stress history information is commonly linked to natural deformation via critical state models and deformation mechanism maps, which are used to assess brittle and ductile deformation mechanisms, respectively. J–T space may be used as a three-dimensional deformation mechanism *space*, wherein both brittle and ductile deformation may be simultaneously related to the stress–temperature path of a rock.

INTRODUCTION

A ROCK is the product of a history of deposition or emplacement, lithification, diagenesis, metamorphism and deformation. As geoscientists, we aspire both to describe the rock in its present state and to assess its history. The investigations of the structural geologist focus primarily on the history and the products of the deformation. Display formats to depict strain or deformation paths (e.g. Flinn 1962) and P–T–t paths have proven to be extremely valuable for understanding and communicating these findings. Stress path analysis, which is the focus of this article, is another important vehicle for visualizing and assessing factors affecting the deformational history.

The deformation of a rock is strongly influenced, sometimes controlled, by the state of stress and the stress history. The Mohr diagram is a graphical display commonly used by geoscientists for discussions of stress state. This display is very useful for the geometric evaluation of a specific stress state, but it is quite awkward for describing or discussing stress history. Though there are a number of alternative graphical displays that are well suited for analysis of stress history (e.g. Jaeger & Cook 1969), most have received only limited attention by the geological community (e.g. Jones & Addis 1986). However, the insight that can be gained from certain of these alternative stress diagrams should warrant a broader utilization.

In the following, the principal graphical formats for stress analysis are described and compared: Mohr space, J space, p–q space and σ space (Fig. 1). Stress history paths (or, simply, stress paths) for various geological scenarios are then presented in the different formats. Finally, a possible coupling of these stress displays with deformation mechanism maps, to link stress paths with observable deformational features, is considered.

STRESS SPACES

The familiar Mohr circle display may be used for either stress or strain. For stress analysis, Mohr space is a two-dimensional space with normal stress (σ_n) and shear stress (τ) as the abscissa and ordinate, respectively (Fig. 1a). A general state of stress is represented by three (semi-)circles, connected along the σ_n-axis at the values of the principal stress magnitudes.

J space, or stress-invariant space, is a two-dimensional space whose abscissa and ordinate are J_1 and $\sqrt{J_2'}$, respectively (Fig. 1b), where (using tensor notation):

$$J_1 = \sigma_{ii} \tag{1}$$

$$\sqrt{J_2'} = (\tfrac{1}{2}\sigma_{ij}'\,\sigma_{ij}')^{1/2} \tag{2}$$

and

$$\sigma_{ij}' = \sigma_{ij} - \delta_{ij}\,\sigma_{kk}/3. \tag{3}$$

J_1 and J_2' are stress invariants (J_1 is the first invariant of stress and J_2' is the second invariant of deviatoric stress). Symmetric second-rank tensors (such as stress and strain) have three invariant values derived from the various components of the tensor. The values of the individual tensor components will, in general, change as the reference co-ordinate system is rotated, but the invariant values do not. For comparison, a vector (which is a first-rank tensor) has one invariant value, viz., the vector magnitude. When expressed in terms of the principal stress values, the J space co-ordinates are:

$$J_1 = \sigma_1 + \sigma_2 + \sigma_3 \tag{4}$$

and

$$\sqrt{J_2'} = \{\tfrac{1}{6}[(\sigma_1 - \sigma_2)^2 + (\sigma_1 - \sigma_3)^2 + (\sigma_2 - \sigma_3)^2]\}^{1/2}. \tag{5}$$

A particular state of stress plots as a point in J space.

Soil mechanics data are commonly presented in p–q space (Fig. 1c; e.g. Jones & Addis 1986, Gens & Potts

1988), which (generally) is defined by co-ordinate axes that are intermediate between those of Mohr space and J space:

$$p = (\sigma_1 + \sigma_2 + \sigma_3)/3 = J_1/3 \quad (6)$$

$$q = \sigma_1 - \sigma_3. \quad (7)$$

A particular state of stress also plots as a point in p–q space.

The co-ordinate axes of three-dimensional σ space are simply the principal stress magnitudes (Fig. 1d). In σ space, any particular state of stress again plots as a point. Note that representation quadrics, e.g. the stress ellipsoid, are sometimes used for the graphic display or analysis of tensor values (e.g. Nye 1972). Though the co-ordinate axes defining the stress ellipsoid are the principal stresses, it is a distinctly different presentation from the σ space described here.

None of these four stress space displays have a direct linkage with the physical (x, y, z) co-ordinate system. However, the Mohr space format does allow a determination of the resolved normal and shear stresses on any plane in physical space, as referenced to the principal stress directions. Neither J space, p–q space nor σ space afford this resolution of the stress values. It is probably this particular capability that has led to the wide usage of the Mohr space format by geologists.

J space is essentially a two-dimensional rendition of σ space. The J_1-axis is defined by $\sqrt{J_2'} = 0$, which is equivalent to $\sigma_1 = \sigma_2 = \sigma_3$. This relationship defines a line (the hydrostat, or **H**) in σ space. Any point or line in J space defines a circle or surface of revolution about **H**, respectively, in σ space (Fig. 2a). The p-axis of p–q space also coincides with **H** in σ space. A particular point in p–q space describes a hexagon of triclinic symmetry (Fig. 2a). It is evident from these relationships that a point in either p–q space or J space represents a family of stress states rather than a unique set of principal stress values.

Critical state models (failure criteria) used to predict the onset of brittle failure or plastic yield are somewhat dictated by the stress space display being used. For rock mechanics and structural geology applications, the Coulomb failure criterion (Coulomb 1776) is used in Mohr space, the Hvorslev surface (Hvorslev 1937) in p–q space, and the Drucker–Prager (Drucker & Prager

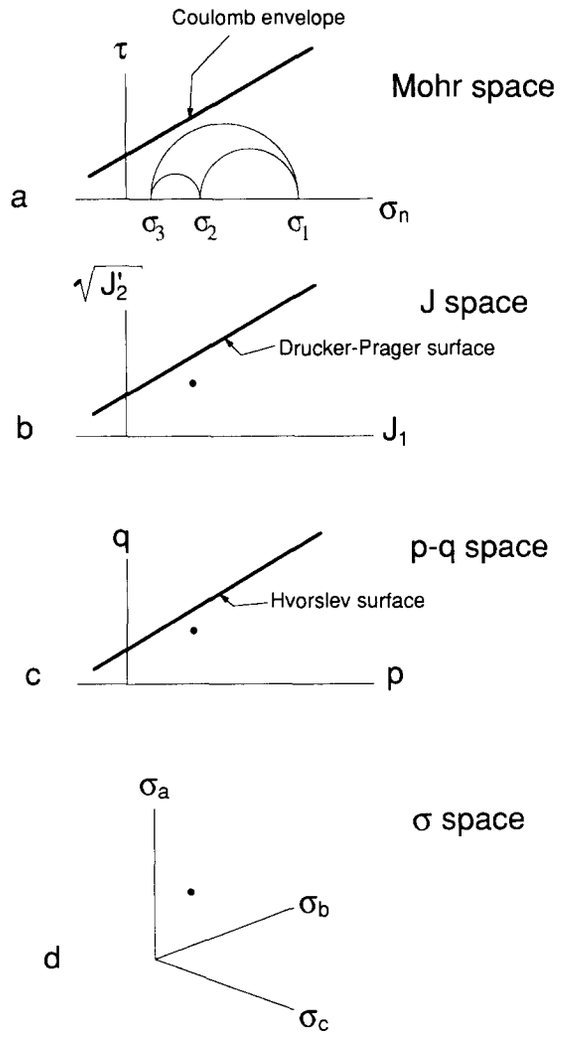

Fig. 1. Various graphic displays for stress analysis: (a) Mohr space; (b) J space, or stress invariant space; (c) p–q space; and (d) σ space. In Mohr space, a general state of stress is represented by three circles (or semicircles). In the other graphics, any particular state of stress is represented by a point.

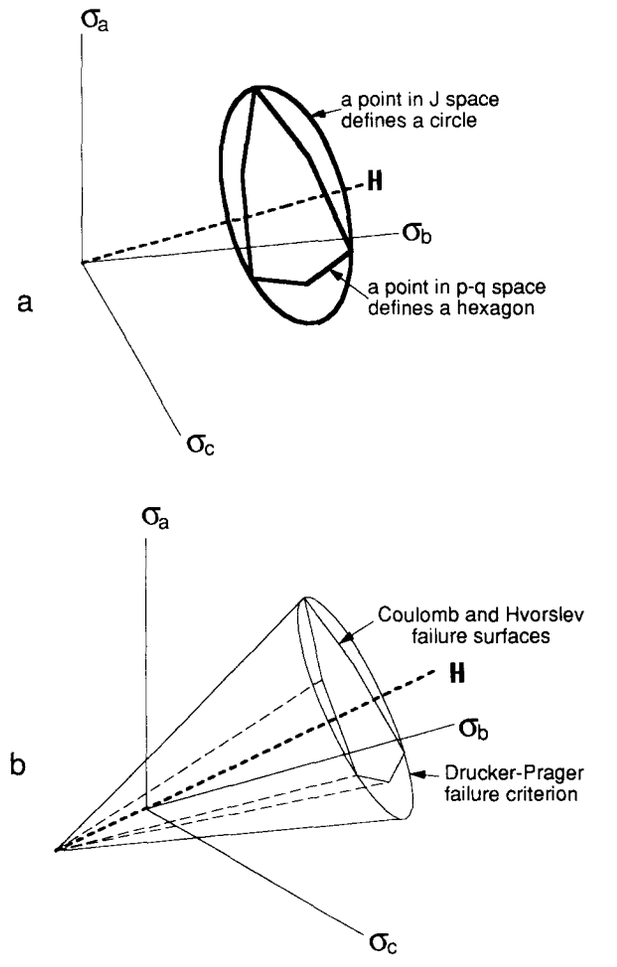

Fig. 2. Relationship between stress data viewed in σ space vs J space and p–q space. (a) A single point in the two-dimensional stress spaces (see Fig. 1) describes a circle or a polygon in the three-dimensional σ space. (b) Failure envelopes for geomaterials which display as single lines in the two-dimensional stress spaces (see Fig. 1), form circular or prismatic cones in σ space.

1952) failure criterion in J space. These several failure criteria, and their non-linear variants, define failure surfaces of basically the same shape in the respective two-dimensional stress spaces (cf. Figs. 1a–c), but they coincide only at a select few points in σ space (Fig. 2b). The distinction between these failure criteria is discussed in more detail, below, in the section on deformation mechanism space.

STRESS PATHS

The relationships between the various stress space displays may be illustrated by considering a relatively simple stress history. Progressive changes in the state of stress will plot as a series of points in J space, p–q space and σ space, defining a line meandering through the different stress spaces. This is the stress path. The corresponding stress changes plot as a series of triple semi-circles in Mohr space. In the following I describe a rock that is: (a) buried to 2 km in a subsiding basin unaffected by any tectonic stresses, then (b) subjected to a regional horizontal contraction (plane strain) followed by (c) an additional 1 km burial, with no additional tectonic loading, and then (d) affected by bending stresses during the incipient phases of plane-strain folding.

The sign convention used throughout this article is + for compression, and all stress terms refer to the effective stress. For this initial example, I assume linear elastic behavior and normal pore pressures, and ignore thermal effects, in order to keep the calculations and concepts simple. In all of the examples, one of the principal stress axes is vertical and the other two lie in the horizontal plane. This allows the stress axes for σ space to be referenced to these particular physical directions, which is convenient for the visualization of the stress path. It should be recognized, though, that this is not the general case, and σ space analysis normally does not permit this physical referencing.

During burial (and subsequently), the vertical stress (σ_v) acting on the rock is the overburden stress (the weight of the overburden less the pore pressure). The horizontal stresses (σ_{h1} and σ_{h2}) associated with burial are calculated using the assumption of uniaxial strain, i.e. the assumption that the body of rock being considered undergoes no lateral contraction or extension during burial:

$$\sigma_{h1} = \sigma_{h2} = \frac{\nu}{1-\nu}\sigma_v, \tag{8}$$

where ν is Poisson's ratio (in this example, $\nu = 0.35$ is used in the initial burial calculation, and $\nu = 0.2$ is used in the subsequent steps).

For progressive burial, the stress history is displayed in Mohr space as a series of circles that become larger and move to the right as the depth of burial increases (Fig. 3a). During this burial phase, the horizontal principal stresses are equal (i.e. $\sigma_{h1} = \sigma_{h2}$), so that the stress at any instant in the burial history plots as a single circle in Mohr space. This burial stress history plots as a linear sequence of points (forming a straight line) in σ space, J space and p–q space (Figs. 4a–c).

During the phase of regional horizontal contraction, the rock is assumed to remain at the same burial depth. The vertical stress is still determined directly from the weight of overburden. Because there is no change in the amount of overburden, there will be no incremental variation (indicated by a Δ preceding the referenced parameter) in the vertical stress:

$$\Delta\sigma_v = 0. \tag{9}$$

However, there will be an increase in both horizontal principal stresses. Equation (9) and the indication that the deformation is plane-strain contraction allows the incremental variations in the horizontal principal stresses to be related:

$$\Delta\sigma_{h2} = \nu\Delta\sigma_{h1}. \tag{10}$$

Because elastic behavior is assumed, no relaxation of existing stresses occurs, and the stresses arising from each phase of the burial and deformation are directly superposed. In Mohr space, the differential increase of the two horizontal stresses produces a series of triple Mohr circles that shift to the right and become progressively larger (Fig. 3b). In σ space, the stress history of this regional contraction is, again, simply a straight line (Fig. 4a), but this same stress history plots as a smoothly varying curve in J space (Fig. 4b) and as a piecewise linear curve in p–q space (Fig. 4c). The nick points in the p–q space stress path occur where the relative magnitudes of the principal stress axes change.

The stress changes associated with the additional phase of burial are governed by the relationships of equation (8). The progressive increase in the principal stress magnitudes is described by a sequence of triple circles in Mohr space (Fig. 3c), a straight line in σ space (Fig. 4a), a curved line in J space (Fig. 4b), and a piecewise linear curve in p–q space (Fig. 4c).

Folding of the strata will produce extension in the outer arc of the fold and contraction in the inner arc. For both cases, the plane-strain assumption produces the relationship between the horizontal stresses shown in equation (10). Because burial depth is not changing during this folding event, there is no change in σ_v (equation 9). In Mohr space, the contraction in the inner arc of the fold produces expanding triple circles moving progressively to the right (Fig. 3d), while the outer arc extension creates a series of circles shifting to the left (Fig. 3e). The stress paths for the inner and outer arc of the fold are, again, straight lines in σ space (Fig. 4a), smooth curves in J space (Fig. 4b) and piecewise linear curves in p–q space (Fig. 4c).

From this simple case study, it can be seen that the complete stress history can be very conveniently displayed and read using the stress paths in either J space or p–q space. Although the stress path is probably most readily understood in the σ space format, this display can be awkward because it is three-dimensional. In contrast,

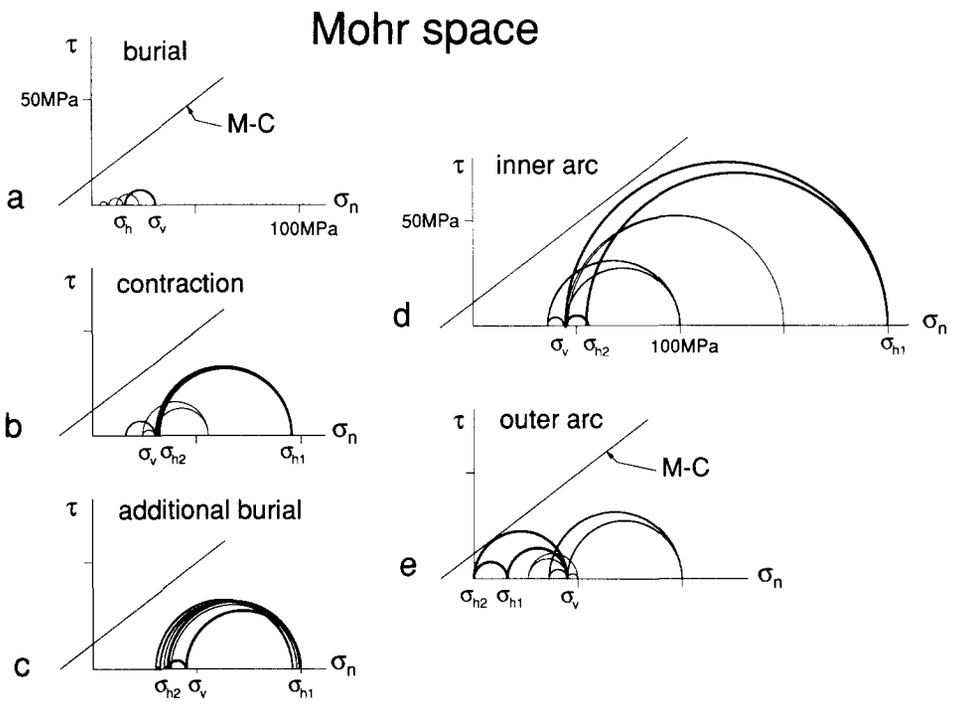

Fig. 3. Mohr space expression of the stress history of a rock (see text for discussion) during (a) uniaxial-strain burial, (b) regional plane-strain contraction, (c) additional burial and (d & e) plane-strain folding. M–C is the Mohr–Coulomb failure envelope. In each diagram, the medium-weight circles represent the stress state at the initiation of the described loading step, the heavy-weight circles represent the final stress conditions for the step, and the light-weight circles represent intermediate portions of the loading path. The principal stress designations on the σ_n axes refer to the final stress conditions (heavy circles) of each loading sequence.

the Mohr space format is conspicuously unsuitable for stress history analysis. Where stress histories are being investigated, Mohr space is most useful as an adjunct to one of the other stress space presentations, e.g. for the resolution of the stresses on particular surfaces or for anticipating the orientation of faults or fractures.

This example has provided a comparative illustration of the different stress space formats. Only σ space and J space will be used in the subsequent stress path discussions.

Burial stress paths

The assumption of *uniaxial elastic strain* for determination of the burial segments of the stress path, used in the above example, represents one extreme of the spectrum of possible burial stress paths (Fig. 5; note that the uniaxial-strain stress path is quite sensitive to the value of ν). The other extreme is represented by *lithostatic* behavior, i.e. $\sigma_{h1} = \sigma_{h2} = \sigma_v$, which produces a stress path along **H** in σ space and along the J_1-axis in J space (Fig. 5). The lithostatic stress path is probably closely approached by clay-rich sediments during their initial phases of burial (i.e. a material that is quite inelastic and that will not support a significant differential stress), whereas a uniaxial elastic strain response would be expected for a rock that is well lithified at the time of deposition, such as a basalt flow. Most other rock types probably experience burial stress paths intermediate between these extremes, as suggested by the heavy dashed line in the two stress spaces (Fig. 5). Any long-term viscous or plastic creep that accommodates a relaxation of the differential stress produced by burial, or other factors, will follow a stress path headed towards the *lithostatic* burial condition (dotted arrow in Fig. 5).

Regional tectonics

The stress paths for the subsidence and uplift components of orogeny may be determined using the concepts and equations for the burial stress path, as presented above. In the following discussion, only the 'non-burial' effects of the regional tectonics are considered, i.e. the stress paths are derived assuming the rock remains at a constant burial depth during the tectonism. Under this assumption, the vertical stress is unaltered by the regional tectonics. Thus, the stress paths, in σ space, all stay in the plane of $\sigma_v = k$ (Fig. 6a), where k is a constant determined by burial depth and pore pressure. It is possible that the principal stress axes may be rotated out of the horizontal plane and the vertical direction by the tectonic deformation, but such rotations are more directly associated with local structural development than with the regional effects.

Regional contraction or regional extension in one direction will alter the horizontal stress in the direction normal to as well as parallel to contraction–extension direction. For plane strain and linear elastic behavior, the incremental changes in the principal horizontal tectonic stresses are governed by equation (10). Purely strike-slip tectonics produces simple shear in the horizontal plane, which yields the relationship

$$\Delta\sigma_{h2} = -\Delta\sigma_{h1}. \qquad (11)$$

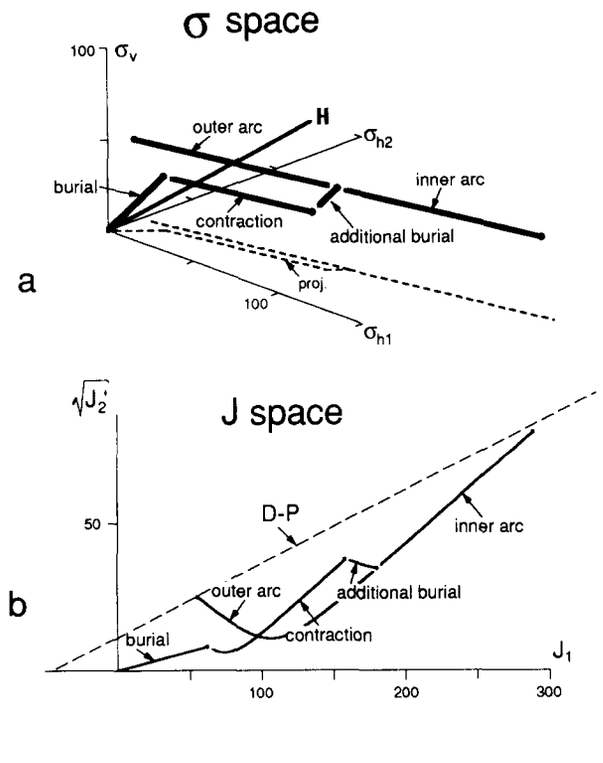

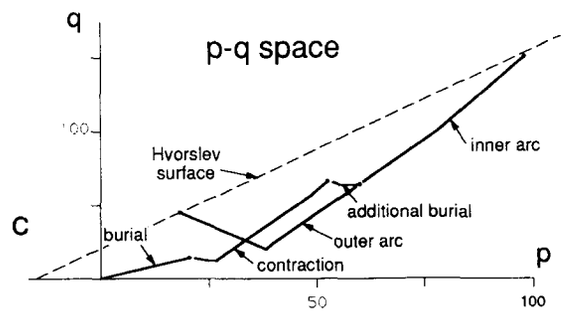

Fig. 4. Stress history of a rock (see text for discussion) as depicted by stress paths in (a) σ space, (b) J space and (c) p–q space. (In all the σ space diagrams, proj. is the projection of the stress path onto the σ_{h1}–σ_{h2} plane. D–P is Drucker–Prager failure surface.)

Transpression and transtension stress paths lie between these end-member paths (Fig. 6).

The path to the failure envelope is much shorter for the extensional setting than it is for contraction (Fig. 6b). Note that the stress path distances to the failure envelope for the strike-slip and transtensive settings are also relatively short (Fig. 6b). The distance to the failure envelope in these various tectonic settings is dominantly controlled by the dependence of the failure envelope on mean stress. Though not elaborated here, variations in the burial stress path (see Fig. 5) will result in an accompanying change in the location and the shape of the subsequent 'tectonic' stress path. Each segment of the stress path, and the resultant deformation, is influenced by the complete stress history.

Pore pressure effects

It is well established that changes in pore pressure (P_p) in a permeable rock will change the effective stress

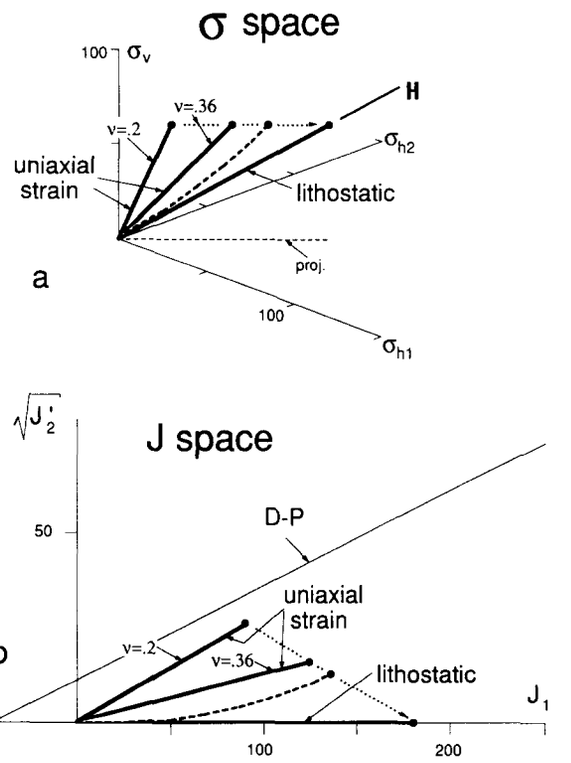

Fig. 5. Stress path in (a) σ space and (b) J space for various burial scenarios. See text for discussion.

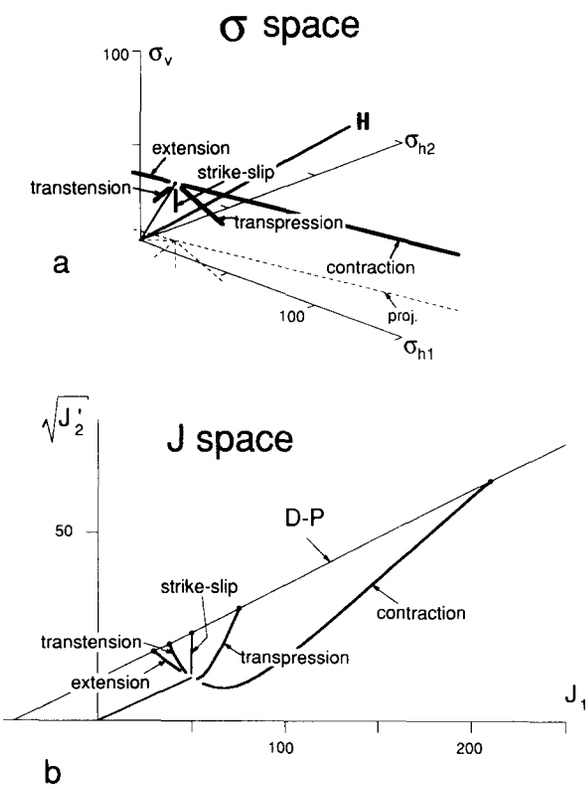

Fig. 6. Stress path in (a) σ space and (b) J space for different regional tectonic settings, as labeled. These regional tectonic stress paths are all for a rock at a constant burial depth during the tectonic loading. Thus, the stress paths all lie in a plane of constant σ_v in (a).

(Hubbert & Rubey 1959, Handin *et al.* 1963). It is commonly assumed that the P_p changes will affect all of the principal stress magnitudes equally (e.g. Handin *et al.* 1963). This will be referenced, in the following, as the assumption of uniform change in the normal stress magnitudes (uniform $\Delta\sigma_n$). In Mohr space, uniform $\Delta\sigma_n$ will shift the position of the center of the Mohr circle, but the diameter (i.e. the differential stress) will be unchanged. In σ space, uniform $\Delta\sigma_n$ produces an effective stress path that is parallel to **H** (Fig. 7a). In J space, uniform $\Delta\sigma_n$ changes J_1 but not $\sqrt{J_2'}$, so the stress path is parallel to J_1, and goes towards the failure envelope for increases in P_p and away from the failure envelope for decreases in P_p (Fig. 7b).

The uniform $\Delta\sigma_n$ assumption is appropriate for a porous body subjected to force boundary conditions (such as a rock in a conventional triaxial testing apparatus). If, however, displacement or mixed boundary conditions are in effect, changes in differential stress (and $\sqrt{J_2'}$) may occur in association with ΔP_p. For a body of rock in the Earth's crust, where lateral movement is restricted by the surrounding rock, the pore pressure effects may be better approximated using the stress relationships for uniaxial strain (Higgs & Bradley 1986). For uniaxial strain and an elastic material response, the effective stress path for ΔP_p will be governed by the relationships of equation (8) and will, thus, be parallel to the uniaxial strain burial stress path (Fig. 7a). (If, more appropriately, the full equations for a thermoporoelastic medium are used, a slight difference will result when the thermal effects are considered, which impact the burial stress path but not the ΔP_p stress path; Higgs & Bradley 1986.) As viewed in J space, the configuration of the ΔP_p stress path (for uniaxial strain) is quite dependent on the state of stress at the inception of the P_p changes (Fig. 7b). In general, increases in P_p will still produce a stress path that goes toward the failure envelope.

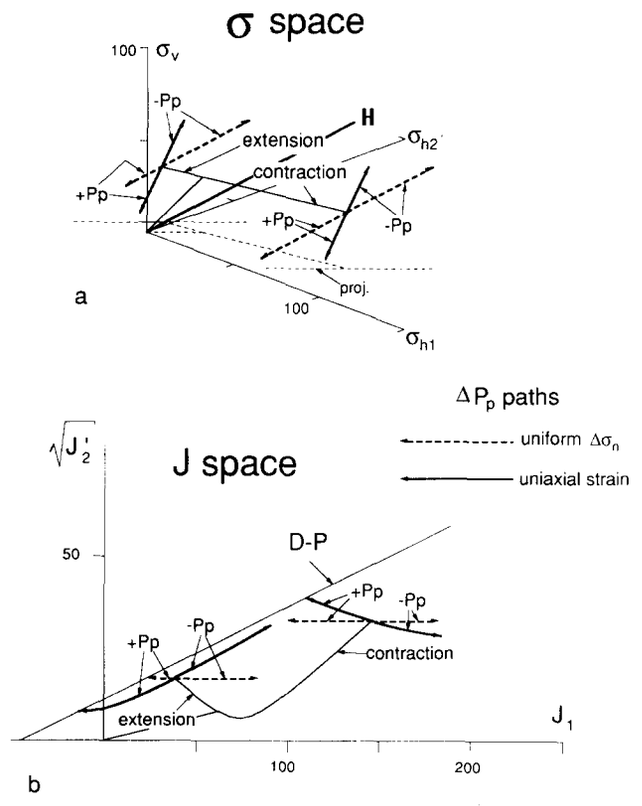

Fig. 7. Stress paths in (a) σ space and (b) J space produced by changes in pore pressure, superposed on stress states representing extensional and convergent tectonic settings. Stress path directions associated with increases in pore pressure denoted by $+P_p$; decreases in pore pressure produce stress paths labeled $-P_p$. See text for discussion of uniform $\Delta\sigma_n$ and uniaxial strain paths.

Rock mechanics stress paths

Our understanding of natural rock deformation has been greatly advanced by studies of the mechanical and deformational behavior of rocks using high-pressure rock mechanics testing apparatus. Most commonly, these tests are conducted on cylindrical samples, with a uniform and constant stress applied perpendicular to the sample axis (the confining pressure, P_c) while the load applied parallel to the sample axis (P_a) is varied, thereby creating a differential stress. In such tests, nominally termed triaxial compression and extension tests, P_a is greater or less than P_c, respectively. The stress paths achieved in these test conditions are restricted, in σ space, to the plane containing P_a and **H** (Fig. 8).

Compared to the variety of possible stress paths that may occur in the natural environment, as illustrated by the preceding examples, these triaxial tests provide a relatively restricted assessment of deformation conditions. Rock mechanicists have long sought to expand the range of testable stress states, using, for example, torsion testing apparatus (e.g. Handin *et al.* 1960) or flat jacks on all sides of a cubic sample (e.g. Reches & Dieterich 1983). These specialized test conditions are technically quite difficult, especially if temperature or P_p are also varied. As a consequence, there exists only a relatively modest amount of rock mechanics information that does not follow the stress paths of the nominal triaxial tests. This point is made here because it is important to realize that the data used to create failure envelopes and deformation mechanism maps, the subjects of the following section, simply do not represent many areas and paths in σ space, or in the other stress

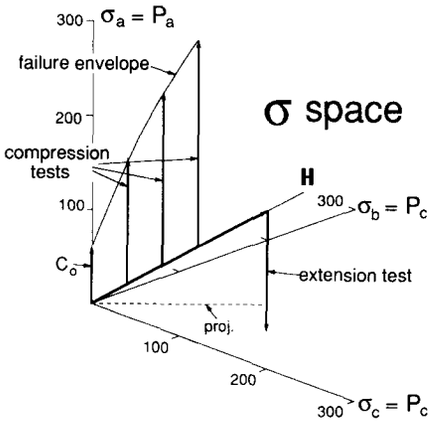

Fig. 8. Stress paths in σ space for conventional 'nominal' triaxial rock mechanics tests. C_o is the stress path for an unconfined (P_c = 1 atm.) or uniaxial *stress* test.

spaces. Consequently, the configuration of failure envelopes and strain rate gradients, presented below and in other literature, should not be considered highly constrained in any stress space.

DEFORMATION MECHANISM SPACE

Stress histories and stress states are useful to the geologist only to the extent that they can be related to geological deformation processes. This linkage is provided by critical state models (failure envelopes, e.g. Coulomb 1776, Drucker & Prager 1952) and deformation mechanism maps (e.g. Rutter 1976, McClay 1977, Chester 1989). In most deformational environments occurring at upper to middle crustal levels, both 'ductile' (used here to indicate temperature and strain-rate dependent processes) and 'brittle' (relatively insensitive to temperature and strain rate) deformation processes occur.

The relative contributions of these various processes to the total deformation will vary as a function of the state conditions and the lithologies involved. Failure envelopes, which anticipate brittle deformation, are usually expressed strictly in terms of stress. Deformation mechanism maps, which primarily address ductile processes, are commonly presented in terms of temperature and some stress factor. Adding a temperature (T) axis to one of the two-dimensional stress displays provides a format for simultaneously relating both brittle and ductile deformation processes to the stress–temperature path. This concept is illustrated, below, for limestone. However, before coupling the two-dimensional stress spaces with temperature, it is appropriate to review the characteristics and limitations of the failure criteria used in the various two-dimensional stress spaces.

The failure envelope

In Mohr space, the failure envelope (see Fig. 1) has the functional form:

$$\tau = \sigma_n \tan \phi + \tau_0, \tag{12}$$

where $\tan \phi$ is termed the coefficient of internal friction and τ_0 is the τ-axis intercept of the failure envelope. This is the Coulomb failure criterion (Coulomb 1776). The counterpart in p–q space is the Hvorslev surface (Hvorslev 1937):

$$q = Mp + B, \tag{13}$$

where M is the slope and B is the q-axis intercept. In J space, the failure envelope has the form:

$$\sqrt{J_2'} = \alpha J_1 + \sigma_y, \tag{14}$$

where α is the slope of the envelope and σ_y is the yield stress for the condition $J_1 = 0$. This is the Drucker–Prager failure criterion (Drucker & Prager 1952). The Drucker–Prager criterion has an explicit dependence on all three principal stress values, the Coulomb (or Mohr–Coulomb, etc.) criterion has no dependence on σ_2, and the Hvorslev surface has an intermediate dependency on σ_2.

These failure criteria are linear relationships for the respective stress spaces. Empirically determined failure envelopes for specific rocks or rock types are usually non-linear (e.g. Jaeger & Cook 1969). In either their linear or non-linear manifestations, these various failure envelopes have comparable geometries in their respective two-dimensional stress space formats (see Fig. 1), but they define quite different failure surfaces in σ space (Fig. 9). The Drucker–Prager failure envelope is a surface of revolution about **H**, i.e. a conical surface in σ space. The Coulomb failure envelope and the Hvorslev surface form identical, triclinically symmetric, prismatic surfaces.

If the conical and prismatic surfaces are established to coincide for triaxial compression test data ($\sigma_2 = \sigma_3$), then a major deviation between the surfaces occurs at $\sigma_2 = \sigma_1$, which is the stress condition obtained in rock mechanics triaxial *extension* tests (Fig. 9a). The actual failure strength of rocks derived from these extension tests falls between these two failure criteria (corresponding triaxial compression and extension test data are shown as solid squares in Fig. 9a). That is, for failure envelopes based on compressional test data, the (Mohr–)Coulomb and Hvorslev failure criteria will underestimate the failure strength in extension and the

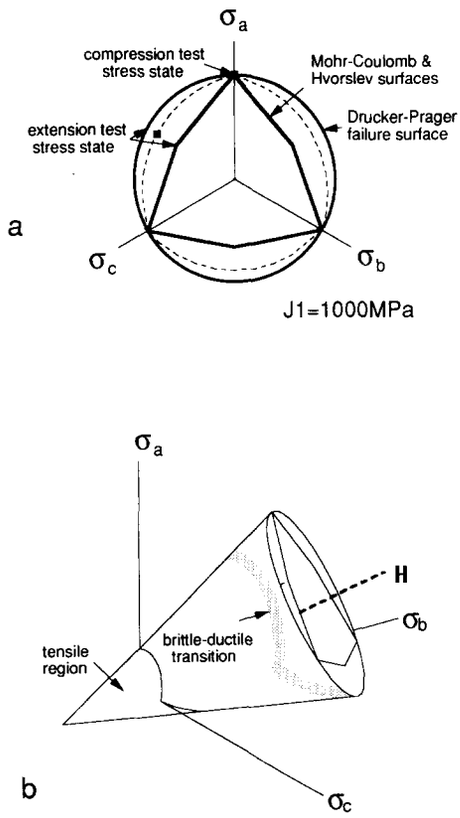

Fig. 9. Configuration of various failure surfaces in σ space (a) in a plane perpendicular to **H** (i.e. in the *deviatoric* plane) and (b) in a perspective view. Relative position of the solid squares in (a) are based on test data of Solenhofen limestone given in Heard (1960). The dashed curve suggests the form of a more accurate general failure surface.

Drucker–Prager failure criteria will overestimate the extensional strength (e.g. Heard 1968). A number of alternative failure criteria have been proposed that more closely approximate three-dimensional critical state characteristics (e.g. the dashed curve in Fig. 9a; see Gens & Potts 1988). These alternative failure criteria, which do not collapse into two-dimensional stress space formats, have received more attention from soil mechanicists than from structural geologists.

There are also other aspects of rock deformation that cannot be fully appreciated in the two-dimensional stress presentations. One example is the transition in brittle deformation from shear fracture to tensile fracture, which occurs, approximately, as the least principal stress shifts from positive to negative (e.g. Griggs & Handin 1960). In σ space, this change in sign of one of the principal stresses occurs when the failure surface crosses any one of the three planes defined by the principal stress axes (i.e. the σ_a–σ_b plane, the σ_a–σ_c plane or the σ_b–σ_c plane, Fig. 9). On the Drucker–Prager failure envelope, this transition from the compressional stress field into the tensile field is scalloped-shaped (Fig. 9b), and is not symmetric about **H** (or J_1). The nominal 'brittle–ductile transition' of rock mechanics tests (which is a function of P_c and is *not* the same brittle–ductile distinction defined above) empirically follows a similarly shaped path on the failure surface (Fig. 9b, e.g. data from Heard 1968). Thus, neither the transition into the tensile stress regime nor the brittle–ductile transition can be delineated as discrete points on the Drucker–Prager envelope in J space (and similarly for the Hvorslev surface in p–q space).

The two-dimensional stress space formats provide a visual and conceptual convenience, but a certain amount of information is lost or overlooked. The above described limitations are not meant to dissuade use of these two-dimensional graphical displays, but rather to illustrate that they *all* have similar shortcomings. The following discussion of J–T space is made with clear cognizance, but without further discussion, of the ambiguities embedded in two-dimensional stress space presentations.

J–T *deformation mechanism space*

A prototype J–T space is formulated for a limestone with a grain size of ~10 μm (Fig. 10). The brittle failure envelope is based on rock mechanics data for the extremely fine-grained Solenhofen limestone (Heard 1960). The failure surface has been reduced 20% (in terms of $\sqrt{J_2'}$) in an attempt to represent the envelope appropriate for geological strain rates (e.g. Costin 1987). The data for dislocation and Coble creep and diffusive mass transfer are derived from the deformation mechanism maps of Rutter (1976), for a grain size of 10 μm, using a shear modulus for calcite of 23 GPa (Birch 1966). Data for twin gliding come from Rowe & Rutter (1990).

Flow laws for dislocation and Coble creep (Rutter 1976) and twin gliding (Friedman 1964) are generally

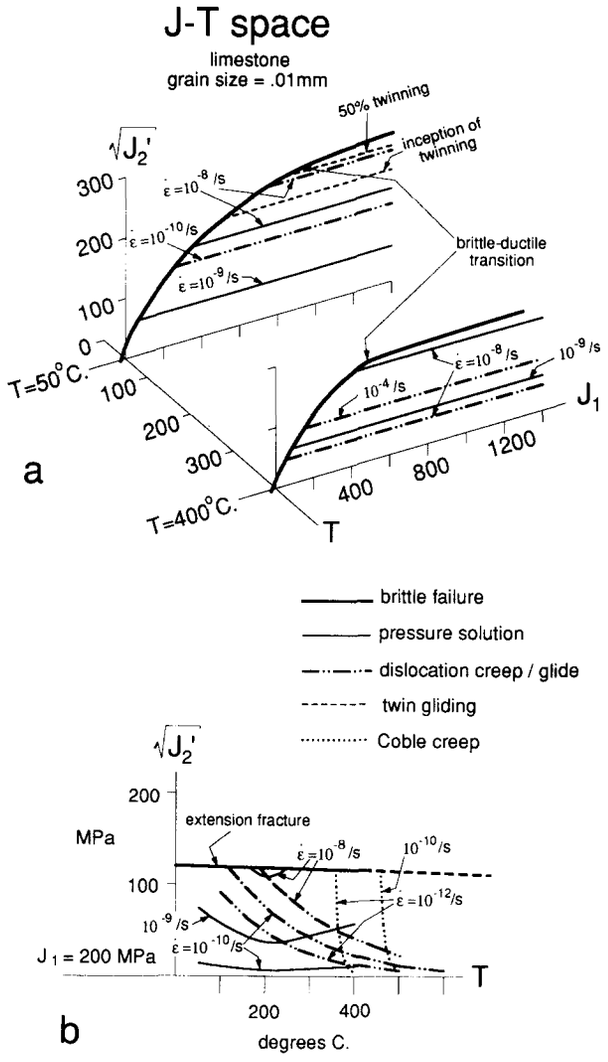

Fig. 10. J–T deformation mechanism space for a limestone with a grain size of 10 μm (see text for discussion). (a) Perspective display of J–T space with slices in the J_1–$\sqrt{J_2'}$ plane shown for temperatures of 50 and 400°C and (b) a slice in the T–$\sqrt{J_2'}$ plane for J_1 = 200 MPa.

formulated to be independent of normal or mean stress. A similar independence is postulated for pressure solution (diffusive mass transfer) mechanisms (Rutter 1976), though the literature is not consistent on this point. Consequently, in any slice through the J–T space perpendicular to T (Fig. 10a), only the brittle deformation envelope shows a variation with J_1. In a slice perpendicular to J_1 (e.g. Fig. 10b), dislocation creep/glide, Coble creep and pressure solution all show a marked variability with T. In this $\sqrt{J_2'}$–T plane, twin gliding is independent of T (Rowe & Rutter 1990), and brittle failure shows only a marginal dependence on T.

Though strain-rate-dependent deformational processes were not considered in the above discussions of stress history, they will influence the stress path. Specifically, they will establish limits to the permissible stress states for a specified lithology and strain rate. For example, if the deformation is occurring at a strain rate ($\dot{\varepsilon}$) of 10^{-8} s^{-1}, the stress can increase in terms of $\sqrt{J_2'}$ until the stress path intersects either the brittle failure surface or a limiting $\dot{\varepsilon}$ gradient (in this case 10^{-8} s^{-1}) for one of the $\dot{\varepsilon}$-dependent deformation mechanisms. In

order for $\sqrt{J_2'}$ to exceed this limiting $\dot{\varepsilon}$ gradient, the $\dot{\varepsilon}$ would have to increase. For $T = 50°C$, the limiting deformation mechanism is pressure solution (see Fig. 10a). At this temperature, if $J_1 < \sim 350$ MPa, the stress path will intersect the brittle failure envelope before it hits any limiting $\dot{\varepsilon}$ gradient. However, for $J_1 > \sim 350$ MPa and $T = 50°C$, the stress path would be limited by the 10^{-8} s^{-1} gradient for pressure solution, and no brittle deformation would occur. Dislocation creep will also occur under these deformational conditions, though at a very subordinate rate to pressure solution, whereas twin gliding would not be initiated.

At $T = 400°C$, dislocation creep becomes the dominant and limiting deformation mechanism at $\dot{\varepsilon} = 10^{-8}$ s^{-1}. Pressure solution will be active as a subordinate process at this temperature, and brittle deformation will occur only at extremely low or negative values of J_1 or at very high (in geological terms) strain rates.

In this extremely fine-grained limestone, for deformation occurring at geologically reasonable strain rates ($\sim 10^{-14}$ to 10^{-12} s^{-1}), brittle deformation would be suppressed at even very low temperatures and J_1 values, as the various $\dot{\varepsilon}$-dependent deformation mechanisms would not permit a significant build up of $\sqrt{J_2'}$. The activity of various deformation mechanisms is very dependent on both mineralogy and grain size. It is specifically the very small grain size of the limestone used in this example that favors pressure solution and certain crystal plastic deformation mechanisms over brittle deformational features. Pressure solution and Coble creep are very sensitive to grain size (Rutter 1976, McClay 1977). If the grain size used for the determination of the strain rate gradients for these mechanisms is increased from 10 to 100 μm, the respective strain rates for the indicated gradients are reduced in value by a factor of 10^{-3} (Rutter 1976; i.e. the $\dot{\varepsilon} = 10^{-8}$ s^{-1} gradient becomes the $\dot{\varepsilon} = 10^{-11}$ s^{-1} gradient, etc.). Compressional strength under confining pressure is, in general, reduced by an increase in grain size. The critical stress for the inception of twinning decreases with increasing grain size (Rowe & Rutter 1990), and dislocation gliding is relatively insensitive to grain size (Rutter 1976).

The specific effect of grain size is illustrated with a comparative J–T deformation mechanism space generated for limestone with a grain size of 0.5 mm (Fig. 11). The brittle failure envelope (based on experimental data for Yule marble, Heard 1968) is about 30% below the failure surface for Solenhofen limestone (in terms of $\sqrt{J_2'}$). Curves for twin development are based on Friedman (1964) and Jamison & Spang (1976). The strain rate values for both the pressure solution and Coble creep gradients will be reduced by a factor of about 10^{-5}. The J–T deformation mechanism space indicates that deformation in this coarse-grained limestone would occur, at upper to middle crustal conditions, by dislocation creep/glide, twinning and brittle failure, with only very minor contributions from pressure solution. The development of twin lamellae in the calcite will provide some record of the stress path (e.g. Jamison & Spang 1976, Rowe & Rutter 1990) and accommodate a certain amount of strain (Groshong 1972), but will not restrict the stress path.

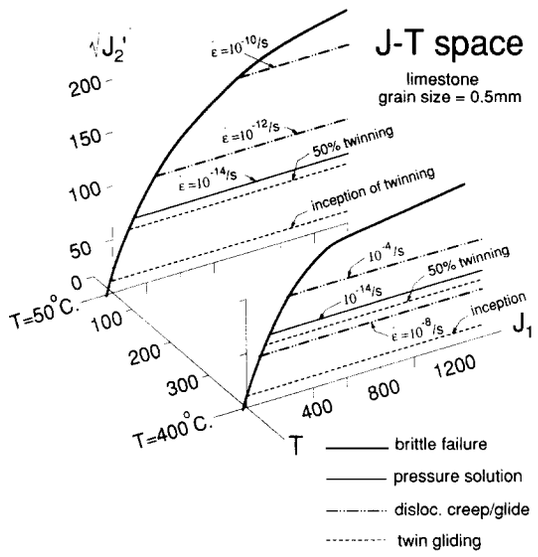

Fig. 11. Perspective display of a J–T space for limestone with a grain size of 0.5 mm, with slices in the J–$\sqrt{J_2'}$ plane shown for temperatures of 50 and 400°C. See text for discussion.

At temperatures of 400°C and greater, brittle deformation under geologically reasonable strain rates would occur in this coarse-grained limestone, as in the finer grained limestone, only at extremely low or negative values of J_1. As the contributions of brittle deformation diminish at the higher temperatures, the three-dimensional complexity of J–T space ceases to provide any benefit over the two-dimensional deformation mechanism maps of Rutter (1976), which is fundamentally a $\sqrt{J_2'}$–T space (e.g. Fig. 10b).

In the stress path discussions of the previous section, it was demonstrated that different points on the same structure can have radically different stress paths (e.g. Fig. 4). In the perspective of these J–T deformation mechanism spaces, it is anticipated that there can also be significant variations in the nature of the deformation as a function of structural position.

CONCLUSIONS

The use of J space, p–q space or σ space as alternatives to the conventional Mohr space presentation for stress analysis allows the stress history of a rock to be clearly represented and visualized. The stress history, which is recorded as a stress path in these various stress spaces, is a function of burial and lithification, regional tectonics, local structural development, pore pressure variations, etc. The cumulative effect of these factors can produce complex stress paths, with resultant stress states that are difficult to anticipate and assess in the absence of these graphical displays.

The power and utility of stress space and stress path analysis for the structural geologists can be realized only if the stress information can be related to mechanisms

and expressions of deformation. Deformation mechanism maps have proven to be very useful for relating ductile deformation mechanisms to state conditions, whereas brittle deformation is correlated to critical state failure envelopes. *J–T* space provides a possible format, a deformation mechanism *space*, for linking both brittle and ductile deformation mechanisms to the stress–temperature history of the rock. The data presently available for the development of a deformation mechanism space for any particular rock type come from a fairly limited range of stress and strain-rate conditions. Consequently, the deformation mechanism spaces presented here (Figs. 10 and 11) should be viewed only as prototypes. Further studies of both natural and experimental rock deformation should provide considerable refinement of such plots.

Acknowledgements—This study was supported by NSERC Operating Grant OGP0105569 to the author. This paper has distinctly benefited from the constructive reviews of Tom Calon, Ramon Loosveld and A. A. M. Venmans.

REFERENCES

Birch, F. 1966. Elastic constants and compressibility. In: *Handbook of Physical Constants* (edited by Clark, S. P., Jr). *Mem. geol. Soc. Am.* **97**, 97–173.

Chester, F. M. 1989. Dynamic recrystallization in semi-brittle faults. *J. Struct. Geol.* **11**, 847–858.

Costin, L. S. 1987. Time-dependent deformation and failure. In: *Fracture Mechanics of Rock* (edited by Atkinson, B. K.). Academic Press, London, 167–215.

Coulomb, C. A. 1776. Essai sur une application des règles de maxims et minims à quelques problèmes de statique, relatifs à l'architecture. *Mém. Acad. R. Sci.* **7**, 343–382.

Drucker, D. C. & Prager, W. 1952. Soil mechanics and plastic analysis of limit design. *Q. Appl. Math.* **10**, 157–165.

Flinn, D. 1962. On folding during three-dimensional progressive deformation. *Q. J. geol. Soc. Lond.* **118**, 385–433.

Friedman, M. 1964. Petrofabric techniques for the determination of principal stress directions in rocks. In: *State of Stress in the Earth's Crust* (edited by Judd, W. R.). Elsevier, New York, 451–550.

Gens, A. & Potts, D. M. 1988. Critical state models in computational geomechanics. *Engng Comput.* **5**, 178–197.

Griggs, D. & Handin, J. 1960. Observations on fracture and a hypothesis of earthquakes. In: *Rock Deformation* (edited by Griggs, D. & Handin, J.). *Mem. geol. Soc. Am.* **79**, 347–364.

Groshong, R. G., Jr. 1972. Strain calculated from twinning in calcite. *Bull. geol. Soc. Am.* **82**, 2025–2038.

Handin, J., Higgs, D. V. & O'Brien, J. K. 1960. Torsion of Yule Marble under confining pressure. In: *Rock Deformation* (edited by Griggs, D. & Handin, J.). *Mem. geol. Soc. Am.* **79**, 347–364.

Handin, J., Hager, R. V., Friedman, M. & Feather, J. N. 1963. Experimental deformation of sedimentary rocks under confining pressure: pore pressure tests. *Bull. Am. Ass. Petrol. Geol.* **47**, 717–755.

Heard, H. C. 1960. Transition from brittle to ductile flow in Solenhofen Limestone as a function of temperature, confining pressure, and interstitial fluid pressure. In: *Rock Deformation* (edited by Griggs, D. & Handin, J.). *Mem. geol. Soc. Am.* **79**, 193–226.

Heard, H. C. 1968. Experimental deformation of rocks and the problem of extrapolation to nature. In: *NSF Advanced Science Seminar in Rock Mechanics* (edited by Riecker, R. E.). Air Force Cambridge Research Laboratories, Bedford, Mass., 439–507.

Higgs, N. G. & Bradley, J. S. 1986. Stress state, fracture development and elastic moduli from microstructural finite element models simulating sedimentary burial. *Eos* **67**, 1205.

Hubbert, M. K. & Rubey, W. W. 1959. Mechanics of fluid-filled porous solids and its application to overthrust faulting. *Bull. geol. Soc. Am.* **70**, 115–166.

Hvorslev, M. J. 1937. Über die Festigkeitseigenschaften gestörter bindiger Böden. Unpublished Ph.D. thesis, Danmarks Naturvidenskabelige Sawfund, Copenhagen.

Jaeger, J. C. & Cook, N. G. W. 1969. *Fundamentals of Rock Mechanics*. Chapman & Hall, London.

Jamison, W. R. & Spang, J. H. 1976. Use of calcite twin lamellae to infer differential stress. *Bull. geol. Soc. Am.* **87**, 868–872.

Jones, M. E. & Addis, M. A. 1986. The application of stress path and critical state analysis to sediment deformation. *J. Struct. Geol.* **8**, 575–580.

McClay, K. R. 1977. Pressure solution and Coble creep in rocks and minerals. *J. geol. Soc. Lond.* **134**, 57–70.

Nye, J. F. 1972. *Physical Properties of Crystals*. Oxford University Press, London.

Reches, Z. & Dieterich, J. H. 1983. Faulting of rocks in three-dimensional strain fields I. Failure of rocks in polyaxial, servo-controlled experiments. *Tectonophysics* **95**, 111–132.

Rowe, K. J. & Rutter, E. H. 1990. Palaeostress estimation using calcite twinning: experimental calibration and application to nature. *J. Struct. Geol.* **12**, 1–17.

Rutter, E. H. 1976. The kinetics of rock deformation by pressure solution. *Phil. Trans. R. Soc. Lond.* **A283**, 203–219.